A unified scenario for the morphology of crack paths in two-dimensional disordered solids

L. Ponson,[1,*] Z. Shabir,[2] M. Abdulmajid,[1] E. Van der Giessen,[3,†] and A. Simone[4,2,‡]

[1] *Institut Jean Le Rond d'Alembert, CNRS - Sorbonne Université, Paris, France*
[2] *Faculty of Civil Engineering and Geosciences, Delft University of Technology, Delft, the Netherlands*
[3] *Zernike Institute for Advanced Materials, University of Groningen, Groningen, the Netherlands*
[4] *Department of Industrial Engineering, University of Padova, Padua, Italy*

(Dated: September 20, 2018)

A combined experimental and numerical investigation of the roughness of intergranular cracks in two-dimensional disordered solids is presented. We focus on brittle materials for which the characteristic length scale of damage is much smaller than the grain size. Surprinsingly, brittle cracks do not follow a persistent path with a roughness exponent $\zeta \approx 0.6$–0.7 as reported for a large range of materials. Instead, we show that they exhibit mono-affine scaling properties characterized by a roughness exponent $\zeta = 0.5 \pm 0.05$, which we explain theoretically from linear elastic fracture mechanics. Our findings support the description of the roughening process in two-dimensional brittle disordered solids by a random walk. Furthermore, they shed light on the failure mechanism at the origin of the persistent behavior with $\zeta \approx 0.6$–0.7 observed for fractures in other materials, suggesting a unified scenario for the geometry of cracks paths in two-dimensional disordered solids.

Keywords: Crack path, roughening processes, scaling properties, fracture mechanisms

I. INTRODUCTION

Deciphering the statistical properties of crack roughness has been a long-standing goal in condensed matter physics [1, 2] driven both by curiosity and the exploration of microscopic failure mechanisms that govern the macroscopic resistance of materials. Here, we evidence a new class of fracture profiles characterized by a random walk behavior that results from a brittle failure mechanism, inviting us to propose a unified scenario for the roughening processes in material failure.

Fracture surfaces reflect the complex interaction of cracks with microstructural material features and therefore represent a ready-made pathway to explore microscale failure mechanisms. The observation of universal scaling behavior on experimental fracture surfaces [3–5] has raised hope that a unified theoretical framework could capture fracture processes in disordered solids. However, such a theory and, more specifically, a quantitative understanding of the scaling properties of fracture surfaces are still missing [6, 7]. To reach these goals, a fundamental issue must first be addressed: most experimental studies of fracture surfaces report large roughness exponent $\zeta \geq 1/2$, classified as persistent profiles, whereas linear elastic fracture mechanics (LEFM) predicts anti-persistent profiles with $\zeta \leq 1/2$ [1, 2, 8]. Here, persistence means that upward (resp. downward) deviations from straightness are more likely to be followed by subsequent upward (resp. downward) deviations.

In three-dimensional (3-D) specimens of metallic alloy [4], mortar [9], wood [10] and quasi-brittle rock [11], fracture profiles display an exponent $\zeta_{3-\mathrm{D}} \simeq 0.75$ that is seemingly incompatible with the LEFM prediction $\zeta_{3-\mathrm{D}} \simeq 0.4$ [12, 13] or with logarithmic correlations [8]. This paradox was partly resolved thanks to the observation in some ceramic and glass of another failure behavior characterized by an exponent $\zeta_{3-\mathrm{D}} \simeq 0.35$–$0.45$ [14–17] or logarithmic correlations [18], in agreement with LEFM [8, 12, 13]. It was then conjectured that anti-persistency (i.e., $\zeta \leq 1/2$) does not reflect the failure behavior of these particular materials but, instead, is a signature of brittle fracture; as such, anti-persistency can be observed in any material, although only at length scales larger than the size ℓ_{pz} of the damage processes localized at the crack tip, thus satisfying the basic assumption of LEFM. This was experimentally confirmed by the observation of two separate scaling regimes: (i) a damage-driven roughness with $\zeta_{3\text{-D}} \approx 0.75$ at scales smaller than ℓ_{pz} and (ii) an LEFM-consistent roughness at larger scales, for a large range of materials including mortar [9], phase-separated glass [18] and metallic alloys [19]. As an interesting application, these results imply that the scaling properties of fracture surfaces can be used to measure the characteristic length scale ℓ_{pz} of the dissipative damage processes accompanying crack growth. This idea, recently tested in simulations [20] and experiments [19], led to the

* laurent.ponson@upmc.fr
† e.van.der.giessen@rug.nl
‡ a.simone@tudelf.nl, angelo.simone@unipd.it

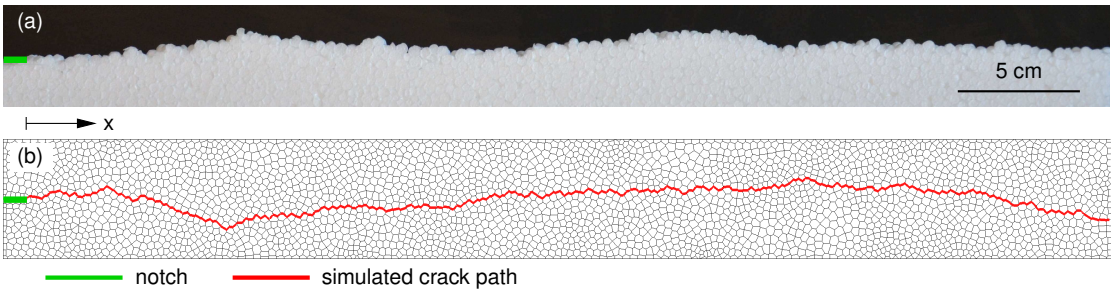

FIG. 1. Brittle intergranular crack profiles obtained from (a) the experimental fracture test of a thin sheet of expanded polystyrene, and (b) the large scale numerical simulation of the cohesive fracture of a random arrangement of polygonal elastic grains.

developement of a new method of material characterization that provides the fracture energy of a material from the post-mortem analysis of its fracture surface [7, 21].

Surprisingly, such a level of understanding is far from being reached for the fracture of two-dimensional (2-D) solids—fracture of 2-D solids arises either when the specimen width is of the same order as the characteristic microstructural size like, e.g., in thin sheets, or when the material microstructure is invariant along the crack front direction. The effective line tension of the crack front resulting from 3-D elasticity that governs the roughening process in the general case [13, 22] does not play any role in 2-D. Instead, the crack propagation direction is controlled by the stress state at the crack tip vicinity, which depends on the local crack inclination and the past trajectory [23–25]. As a result, the response of an advancing crack to small perturbations of its path is essentially different in 2-D and 3-D.

In general, brittle cracks in homogeneous media recover a straight trajectory after any small perturbations. Consequently, LEFM based models of crack propagation in disordered 2-D solids predict anti-persistent fracture profiles, with $\zeta_{2\text{-D}} \leq 0.5$ [8], or even no self-affine regime at all [26, 27]. These predictions are in contradiction with experiments that systematically report exponents in the range $\zeta_{2\text{-D}} \approx 0.6$–$0.7$ as in paper sheets [28–30], wood [31] or nickel-based alloy [32]. Recent numerical studies that take into account the nucleation, growth, and coalescence of voids during the failure of 2-D solids report values in the range $\zeta_{2\text{-D}} \approx 0.65$–$0.7$ that are close to those obtained in experiments [33, 34]. These findings are also consistent with the numerical observations made in random fuse and random beam models that describe failure as a microcrak coalescence process [35, 36]. Overall, these results suggest that the persistency observed on fracture profiles is reminiscent of crack growth by void coalescence, like in 3-D. But does this mean that crack paths in 2-D solids are systematically driven by void coalescence, or can another behavior compatible with LEFM be observed? If it exists, what are the geometrical features of the resulting fracture profiles that have recently been a matter of debate [26, 27]? Last but not least, how would one roughening mechanism be selected over the other? A crack growth regime compatible with LEFM represents the missing piece for explaining crack trajectories in heterogeneous materials. Therefore, exploration of this regime by experimental and numerical means is the central point of this study.

To address this challenge, we consider 2-D consolidated granular materials characterized by intergranular failure that have been used in the past as archetypes of disordered brittle materials [12, 15]. Their fracture profiles are investigated experimentally in non-porous thin sheets made of consolidated polystyrene beads and numerically in large scale 2-D simulations of cohesive zone fracture of random arrangements of polygonal grains, both shown in Fig. 1. They are shown to display surprisingly simple properties that cleary distingish them from the persistent fracture profiles reported so far. In the last part, we take inspiration from Refs. [26, 27] and propose a model of crack propagation through disordered brittle solids that sheds light on our findings. Our study suggests a unified scenario for the morphology of fracture paths in 2-D disordered solids that is discussed in the concluding section.

II. METHODS

A. Experimental fracture tests of two-dimensional granular solids

To explore the fracture profiles formed by brittle intergranular failure, we use commercial panels of expanded polystyrene from which fracture testing samples are machined. Each panel consists of consolidated pre-expanded polystyrene beads with an average radius $\ell \simeq 2$ mm. The radius of the beads is comparable to the panel thickness but is two to three hundred orders of magnitude smaller than the other dimensions of the specimens. The material Young's modulus, measured through uni-axial tensile test, is $E = 6.5 \pm 0.5$ MPa while its fracture energy, obtained from the

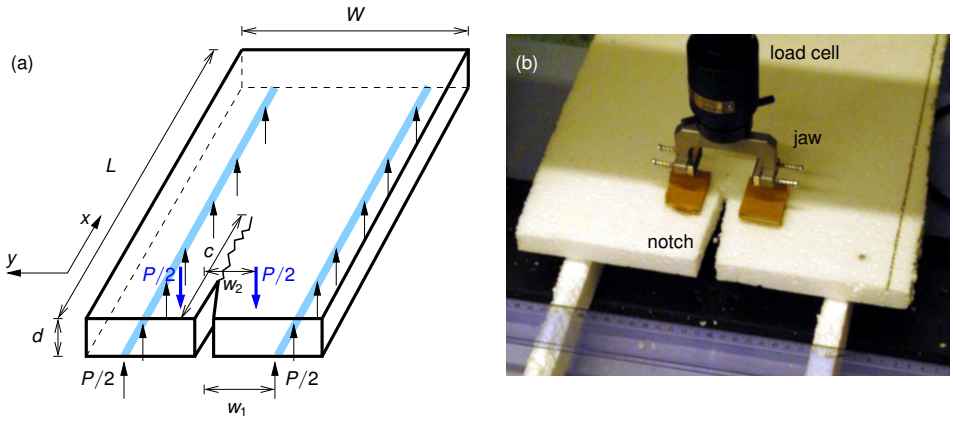

FIG. 2. Experimental setup used in the first series of fracture tests realized to investigate the crack path: (a) schematic representation of the fracture sample and the boundary conditions; (b) pre-notched specimen and loading device.

fracture tests described next, is $G_c = 60 \pm 3$ Jm^{-2}. An estimate of the cohesive stress between individual grains is obtained from uniaxial tensile tests with blunt notch of different tip radii [37], leading to $\sigma_c = 0.6 \pm 0.1$ MPa. A cohesive zone model like the one by Barrenblatt [38] provides the characteristic size $\ell_{pz} = \pi G_c E/(8\sigma_c^2) \simeq 0.45 \pm 0.20$ mm of the process zone where damage mechanisms localize in the crack tip vicinity. The cohesive length ℓ_{pz} is found to be much smaller than the grain size ℓ, suggesting that the polystyrene panels used in this study can be safely approximated by a brittle cohesive granular solid.

Two different fracture test geometries are considered. In the first series of experiments, the so-called double torsion test, with sample dimensions $W \times L \times d = 30$ cm $\times$ 60 cm $\times$ 1.5 cm and notch length $c_0 = 10$ cm, is used. The sample is schematically shown in Fig. 2(a). This geometry is used in experimental fracture mechanics to achieve slow and controlled mode I crack propagation under tensile loading conditions in thin specimens [39, 40]. In general, a groove carved in the specimen upper surface is required to guide the crack parallel to the initial notch. In our setup, however, straight crack propagation was achieved without a groove by properly choosing the location of the applied forces. Two point forces are applied from the top of the specimen on each side of the notch at a distance $w_2 = 2.5$ cm from it. Two parallel rails support the specimen from the lower side at a distance $w_1 = 10$ cm from the notch. In order to avoid indentation of the specimen, the upper jaws are not directly in contact with the upper face of the sample, but apply a distributed force over an area of about 5 cm^2 thanks to a thin plate placed between the jaw and the specimen as shown in Fig. 2(b). The upper jaw is displaced vertically at a constant velocity $v_{ext} = 0.1$ mm/s, leading to slow crack propagation until full failure of the specimen. During the test, the crack propagates over a total distance $\Delta c \simeq 50$ cm that corresponds to about 250 polystyrene beads, thus allowing for a rather extended length scale range to investigate the scaling properties of the crack path (see Fig. 6). In the second series of mode I experiments, the so-called thin strip geometry, with sample dimensions $W \times 3W \times 1.3$ mm and notch length $2W/3$, is used. The sample is schematically represented in Fig. 3(a). Opening stresses are applied through uniform displacements imposed along the specimen thanks to two couples of long metallic strips that are firmly clamped to the polystyrene sheet in its lower and upper region (see Fig. 3(b)). The strips are attached to the mechanical test machine through U-shape jaws. The upper jaw is displaced vertically at a constant velocity $v_{ext} = 0.1$ mm/s, leading to slow crack propagation until full failure of the specimen. This geometry has been largely used to study slow mode I fracture thanks to its ability to propagate straight cracks with controlled speed under displacement controlled conditions. Our aim is to investigate the effect of the sample size on the geometry of the fracture profiles. As a result, several specimen widths W ranging between 75ℓ and 260ℓ are investigated, while keeping the sample aspect ratio constant.

After failure, crack profiles are extracted using digital image analysis of pictures of the broken sample, an example of which is shown in Fig. 1(a).

B. Simulations of intergranular failure

Intergranular crack propagation in any consolidated granular material with zero porosity can be adequately modeled under the assumption that dissipative failure processes are confined to grain boundaries. Crack paths are obtained using a generalized finite element method for polycrystals [41], a method in which a polycrystal is obtained by the superposition of a polycrystalline topology on a background finite element mesh with no need to generate meshes conforming to the microstructure. Additionally, the method can deliver an accurate description of the stress field

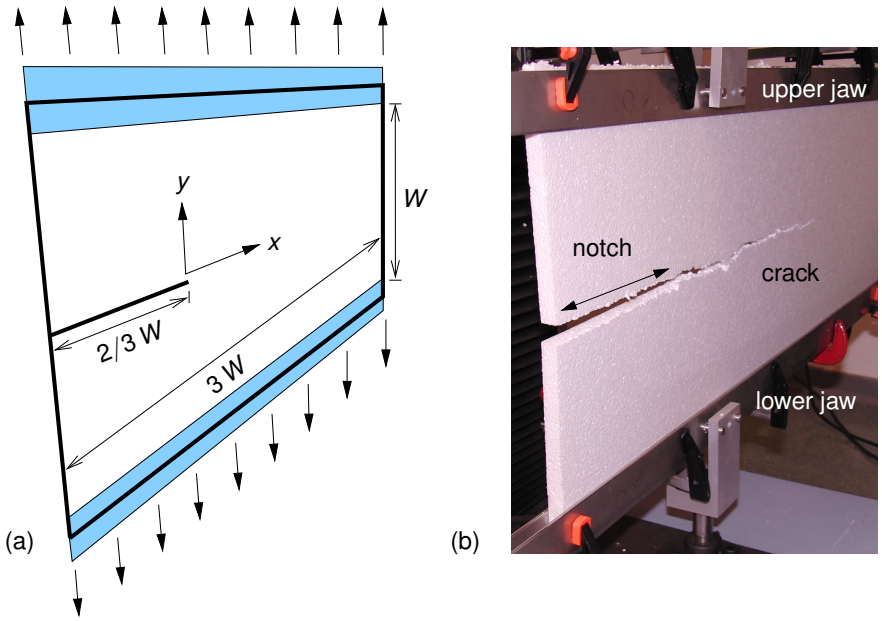

FIG. 3. Experimental setup used in the second series of fracture tests to investigate the effect of the specimen size on the crack roughness geometry: (a) schematic representation of the sample and the boundary conditions; (b) broken specimen and loading device.

around a propagating crack tip in polycrystalline materials and reliable crack paths [42].

A representative example of the Voronoi microstructures considered in this study is shown in Fig. 1(b). These microstructures are embedded in the numerical process zone of the specimen in Fig. 4. The material parameters are taken to be representative of an average polycrystalline alumina, Al_2O_3, with Young's modulus $E = 384.6$ GPa and Poisson's ratio $\nu = 0.237$. An average grain size of approximately 20 μm has been used; this size corresponds to an average grain boundary length $\ell = 10.62$ μm. The number of grain boundaries ahead the notch tip is around 320 on average. Plane strain analyses are performed under the assumption of small elastic strains and rotations.

The linear elastic isotropic grains are connected to each other by means of cohesive grain boundaries that follow the Xu-Needleman cohesive law [43] incorporating secant unloading and reloading behavior. As shown by Shabir *et al.* [42], intergranular crack paths in brittle polycrystals are unique for a given microstructure, irrespective of cohesive law parameters. Using therefore the parameter set in Ref. [42], and with the mode I fracture energy $G_{\rm Ic} = 39.6$ Jm^{-2} and the maximum normal cohesive strength $\sigma_{\rm max} = 0.6$ GPa, a relatively coarse discretization can resolve the cohesive zone along a grain boundary. The determination of the roughness exponent however calls for crack paths obtained from polycrystalline aggregates with a large number of grains (Fig. 1(b)). Even with the meshing requirements that come with the choice of the cohesive law parameters just described, the resulting simulations cannot be conveniently handled using traditional fully resolved monolithic analyses. To solve this problem, we have developed a simple sequential polycrystalline analysis approach in which the cohesive zone along a grain boundary is resolved only for the grains in a region around the propagating crack tip. In this approach, detailed and validated in Appendix A, a simulation is split into a suitable number of sub-simulations. At the beginning of the first sub-simulation, a process window (the leftmost region enclosed by the blue box in Fig. 5 and appropriately discretized) encloses the notch and the region where the crack will most likely propagate. The specimen is loaded by a uniform tensile stress, σ, ramped incrementally under quasi-static loading conditions. When the crack tip approaches the boundary of the process window, the sub-simulation is stopped and the simulation data are stored on a file. In the next sub-simulation the previous simulation data are loaded, and the new process window contains the crack tip from the previous sub-simulation, its corresponding non-linear region, and the region where the crack will most likely propagate. As in the previous sub-simulation, the load is applied incrementally until the crack reaches the boundary of the process window. This procedure is repeated until the specimen is fully cracked.

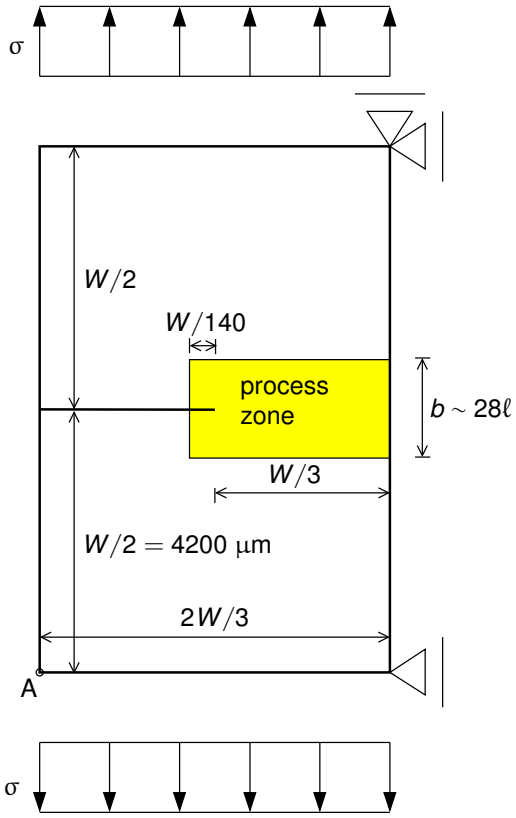

FIG. 4. Geometry and boundary conditions of the notched specimen employed in the simulations.

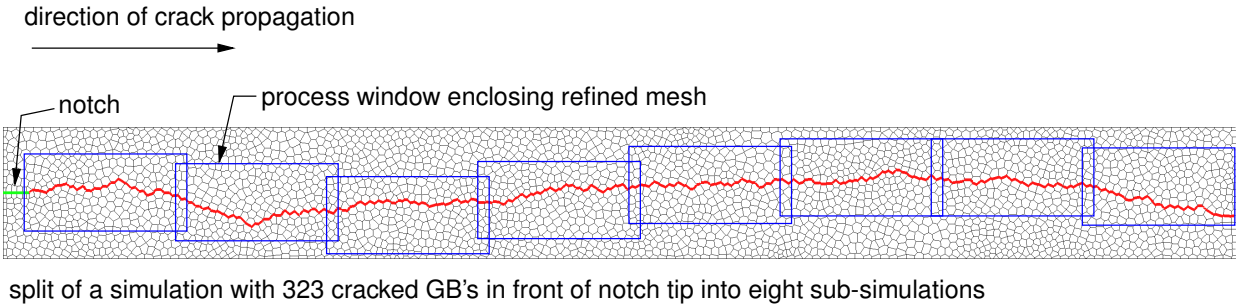

FIG. 5. Sequential polycrystalline analysis of the 3140-grain topology in Fig. 1(b). Only the process zone, rotated by $-90°$, is shown.

III. ROUGHNESS CHARACTERIZATION OF THE CRACK PROFILES

A. Scaling properties

The statistics of experimental and computed crack profiles are now investigated. We start by computing the correlation function $\Delta h(\delta x) = \langle [h(x+\delta x) - h(x)]^2 \rangle_x^{1/2}$ of the crack roughness profile h, where δx is the increment in the spatial coordinate x. In view of sample-to-sample stochastic variations, $\Delta h(\delta x)$ is averaged over six experimental crack profiles obtained from double torsion tests and 18 simulated profiles. In the simulations, the grain arrangements consist of 3140 grains (Fig. 1(b)) obtained with a centroidal Voronoi tessellation algorithm. Figure 6 shows the correlation functions of experimental and computed profiles. Both follow a power-law relation $\Delta h(\delta x) \propto \delta x^{\zeta}$, which is reminiscent of self-affine properties characterized by a roughness exponent $\zeta_{\text{exp}} = 0.48 \pm 0.03$ for the experiments and $\zeta_{\text{sim}} = 0.50 \pm 0.02$ for the simulations (the standard errors are obtained from the roughness exponents computed on each profile analyzed separately). The self-affine behavior extends two decades ($\approx 100\,\ell$) beyond the characteristic

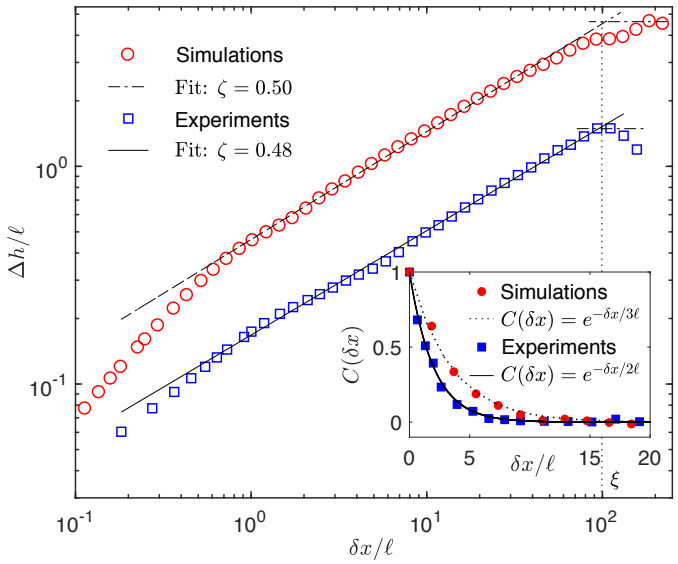

FIG. 6. Logarithmic representation of the height correlation function of the experimental and computed crack profiles. At scales larger than the microstructural length ℓ (bead radius in the experiments and grain boundary length in the simulations), the crack roughness is self-affine with an exponent $\zeta \simeq 0.5$. The inset shows that the correlator of the crack local slopes decays exponentially fast over a few ℓ, confirming the random walk behavior.

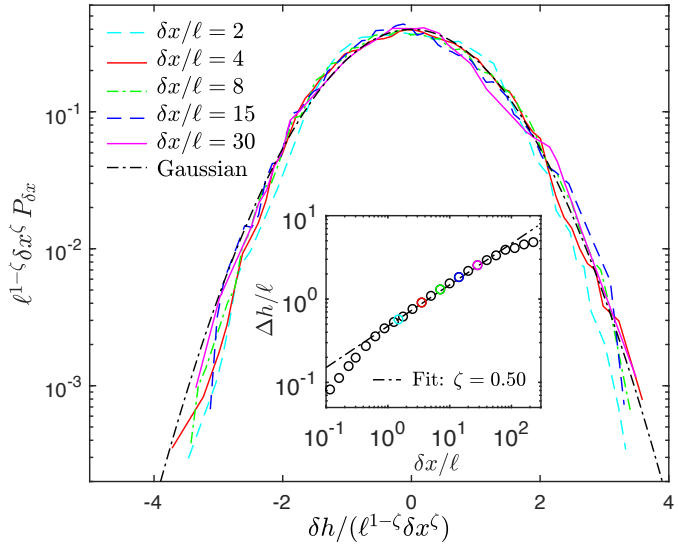

FIG. 7. Statistical distribution $P_{\delta x}$ of height variations computed for different scales δx. After normalization by δx^{ζ} with $\zeta = 0.5$, they collapse to a Gaussian distribution. The inset shows that the studied values of δx belong to the self-affine domain $1 \lesssim \delta x/\ell \lesssim 100$.

microstructural length ℓ (bead radius in the experiments and grain boundary length in the simulations). The value of the roughness exponent close to the directed random walk exponent $\zeta_{\rm rw} = 1/2$ is confirmed by the behavior of the function $C(\delta x) = \langle h'(x+\delta x)h'(x)\rangle_x / \langle (h'(x))^2\rangle_x$ that, according to the inset of Fig. 6, shows no correlation of the crack local slopes $h' = {\rm d}h/{\rm d}x$ on length scales $\delta x \gg \ell$.

We take advantage of the large number of long fracture profiles produced by the simulation to study the full statistics of their roughness. The distributions $P_{\delta x}$ of the height fluctuations $\delta h = h(x+\delta x) - h(x)$ computed at some scale δx are shown in Fig. 7. When normalized by δx^{ζ} with $\zeta = 0.5$, the distributions corresponding to different values of δx collapse to the same master curve, thus reflecting a mono-affine behavior. Mono-affinity is ensured as long as δx belongs to the self-affine domain, as shown in the inset. Note also that the roughness statistics is Gaussian, as evidenced by the characteristic parabolic shape of $P_{\delta x}(\delta h)$ shown in Fig. 7.

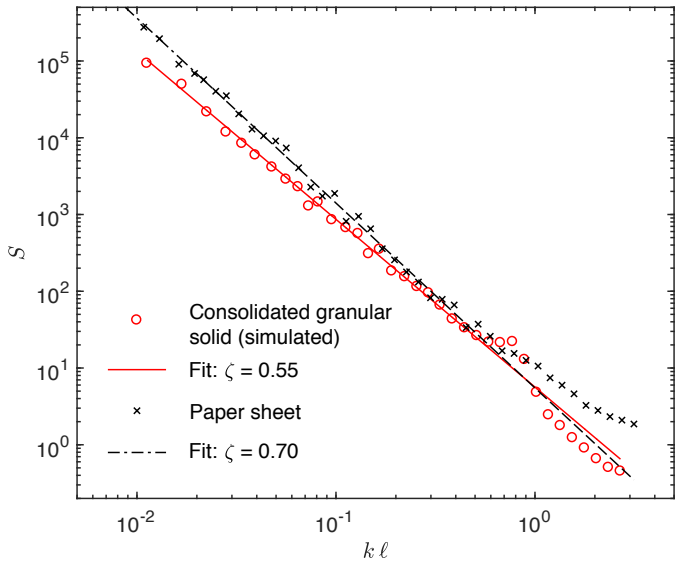

FIG. 8. Power spectrum $P_{\delta x}$ of simulated fracture profiles in 2-D polycrystals and comparison with experimental fracture profiles in paper sheets (from Refs. [7, 45]). The power law behavior $S(k) \sim k^{-1-2\zeta}$ with $\zeta = 0.55$ confirms the estimate of the roughness exponent obtained in the direct space in Fig. 7: it is significantly smaller than the roughness exponent $\zeta = 0.7$ characterizing fractured paper sheets. The length scale ℓ used to normalize the wavenumber $k = 2\pi/\lambda$ is taken as the grain size for the polycrystal and the characteristic microstructural scale (like, e.g., the fiber length) $\ell \simeq 1$ mm for the paper sheet.

To confirm the value of the roughness exponent ($\zeta \simeq 0.5$), we use an independent method to analyze the simulated fracture profiles based on the calculation of their Fourier transform [44]. Figure 8 shows the spectral density of the fracture profiles defined as

$$S(k) = |\tilde{h}(k)|^2 \quad \text{with} \quad \tilde{h}(k) = \frac{1}{2\pi} \int f(x) e^{-ikx}\, \mathrm{d}x. \tag{1}$$

The observed power law behavior $S(k) \sim k^{-1-2\zeta}$ with $\zeta = 0.55$ is compatible with the previous estimate based on the scaling $\Delta h \sim \delta x^{\zeta}$ of the correlation function (see Fig. 6).

To provide a direct comparison with other 2-D materials, the spectral density of fracture profiles obtained in paper sheet that has been studied in Refs. [7, 45] is also shown in Fig. 8. The difference with the behavior of cracks in polycrystalline solids as studied here emerges clearly: the crack profiles in paper show an excess of long wavelength modes observable for $k\,\ell \ll 1$ that reflects in a larger value of the roughness exponent $\zeta \simeq 0.7$. These modes, more abundant in fractured paper sheets than in fractured granular solids, are reminiscent of the persistent behavior of cracks in paper sheets. Indeed, persistence means that an upward (resp. downward) deviation is more likely followed by a subsequent upward (resp. downward) deviation, thus building-up long wavelength perturbation modes. By contrast, the roughness exponent close to $\zeta_{\mathrm{rw}} = 1/2$ indicates that cracks in 2-D consolidated granular solids follow paths close to a directed random walk, i.e., without significant correlations in the sign of successive growth increments.

To be more precise, the difference between the geometry of these fracture profiles goes well beyond the value of the roughness exponent. Fractured paper sheets display non-Gaussian fluctuations of height with fat tails [46] that contrast with the Gaussian behavior reported in Fig. 7. They also exhibit multi-affinity: different roughness exponents $\zeta(q)$ are required to describe the scaling behavior of the various moments $\langle [h(x+\delta x) - h(x)]^q \rangle_x^{1/q} \sim \delta x^{\zeta(q)}$ of the height fluctuations [46], while one exponent only, $\zeta \simeq 0.5$, describes the full statistics of brittle crack path.

To characterize further their scaling properties, we now investigate the effect of the size of the fractured specimen on the resulting fracture profiles.

B. Effect of specimen size on the roughness scaling properties

The correlation function of the crack profiles represented in Fig. 7 shows that the self-affine regime extends from the grain size up to some characteristic length scale $\xi \simeq 100\ \ell$. What is the origin of this upper limit? To address this question, we perform a series of fracture tests using the thin strip geometry described in Fig. 3 with various widths

in the range $150 \leq W/\ell \leq 520$ while keeping the ratio between W and the other samples dimensions (such as length and notch length) constant. The height-height correlation functions of the fracture profiles corresponding to different widths W are shown in Fig. 9. They show a self-affine behavior with an exponent $\zeta \simeq 0.5$, irrespective of the specimen dimension. However, the range of length scales $\ell \lesssim \delta x \lesssim \xi$ over which power law behavior is observed clearly increases with increasing width W. The effect of the upper bound ξ of the self-affine domain (as defined in Fig. 6) is studied quantitatively in the inset of Fig. 9, revealing a linear relationship ($\xi \simeq 0.4\, W$) between both length scales. In other words, the finite domain of the roughness scaling behavior is a consequence of the finite size of the fractured specimen. As the sample size increases, the wavelength ξ of the largest perturbations of the crack trajectory increases too. This behavior is analogous to that reported in fractured 3-D brittle solids: there, the upper bound of the self-affine regime with exponent $\zeta_{\text{3-D}} \simeq 0.4$ also scales linearly with the specimen size [47] but differs from the scaling properties of fractured quasi-brittle and ductile solids with exponent $\zeta_{\text{3-D}} \simeq 0.8$ that are bounded by the process zone size. The latter is a material characteristic length scale that is independent of specimen size.

The properties of the experimental and simulated fracture profiles observed in consolidated granular solids lead to several questions. Where does the roughness exponent $\zeta \simeq 0.5$ emerge from, while crack trajectories in other 2-D disordered solids show persistence with $\zeta \simeq 0.7$? And can we rationalize the Gaussian and mono-affine statistics of brittle crack paths as opposed to the properties of fracture profiles reported so far in 2-D solids?

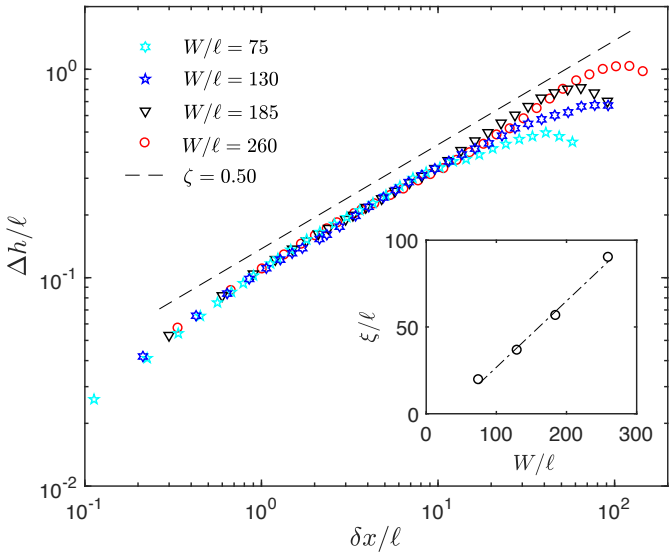

FIG. 9. Logarithmic representation of the height correlation function of the experimental fracture profiles obtained from the thin strip geometry for various specimen widths W (see Fig. 3). The crack profiles are self-affine with an exponent $\zeta \simeq 0.5$, up to some cut-off ξ that depends on the sample size. The inset shows that the upper bound ξ of the self-affine regime increases linearly with the sample width.

IV. THEORETICAL INTERPRETATION

To address these issues, we study, theoretically, the trajectory followed by a crack in a two-dimensional elastic solid with disordered fracture properties and uniform linear elastic properties. Our model builds on basic concepts of LEFM and more specifically on the principle of local symmetry [23, 48] that predicts cracks propagation along the direction of vanishing shearing mode II—note that even though the specimens considered in our study may be loaded in pure mode I tension at the structural scale, the perturbations of the crack profile at the microstructural scale result in some local shearing in the crack tip vicinity. Following Katzav *et al.* [26, 27], we describe the crack path $h(x)$ as a succession of straight segments of size δx along the average propagation direction x that are taken in the limit $\delta x \to 0$. We start from the results by Cotterel and Rice [23, below Eq. 43] according to which the kink angle between two successive incremental steps is given by

$$h'(x^+) - h'(x^-) = -2\frac{k_{\text{II}}(x)}{k_{\text{I}}(x)}, \tag{2}$$

	sign (T)	$\mathcal{L}_1$	sign (A)	$\mathcal{L}_2$
Simulations	-1	$85\,W = 85000\,\ell$	-1	$W/3 = 330\,\ell$
Double torsion experiments	-1	$\simeq L^2/W \simeq 600\,\ell$	-1	$\simeq W/2 \simeq 75\,\ell$
Thin strip experiments	1	$\simeq W$	-1	$\simeq W/2$

TABLE I. Structural length scales $\mathcal{L}_1$ and $\mathcal{L}_2$ and signs of the T-stress and the parameter A that appear in the crack path equation (5). The finite element method analyses used to compute them are described in Appendix B.

where h' indicates $\mathrm{d}h/\mathrm{d}x$. The kink angle is defined as the difference between the propagation direction after and before the kink, as done in [24]. The local stress intensity factors $k_{\mathrm{I}}(x)$ and $k_{\mathrm{II}}(x)$ are calculated from the crack path configuration before the kink. Since we limit our analysis to slightly perturbed cracks for which $h' \ll 1$, we can use the results of Cotterel and Rice [23] complemented by those of Movchan *et al.* [49]. These results provide the local stress intensity factors $\{k_{\mathrm{I}}^{\mathrm{hom}}, k_{\mathrm{II}}^{\mathrm{hom}}\}$ for a homogeneous material as a function of the past trajectory $h(\tilde{x} < x)$, the macroscopic stress intensity factors $\{K_{\mathrm{I}}, K_{\mathrm{II}}\}$ imposed by the loading machine to the specimen, and the coefficients $\{T, A\}$ of the higher order terms in the Williams' development of the stress field near the crack tip [50]:

$$\left\{\begin{array}{rcl} k_{\mathrm{I}}^{\mathrm{hom}}(x) & = & K_{\mathrm{I}} \\ k_{\mathrm{II}}^{\mathrm{hom}}(x) & = & K_{\mathrm{II}} + \dfrac{K_{\mathrm{I}}}{2} h'(x^-) - \sqrt{\dfrac{\pi}{2}} A h(x) \\ & & -\sqrt{\dfrac{2}{\pi}}\, T \displaystyle\int_{-\infty}^{x} \frac{h'(\tilde{x})}{\sqrt{x-\tilde{x}}}\,\mathrm{d}\tilde{x}. \end{array}\right. \tag{3}$$

Since in this study the macroscopically applied shearing K_{II} is zero, the combination of Eqs. (2) and (3), with $k_{\mathrm{II}}(x) = k_{\mathrm{II}}^{\mathrm{hom}}(x)$ for a homogeneous material, yields the following closed form of the path equation:

$$h'(x^+) = \frac{2\sqrt{2}}{\sqrt{\pi}} \frac{T}{K_{\mathrm{I}}} \int_{-\infty}^{x} \frac{h'(\tilde{x})}{\sqrt{x-\tilde{x}}}\,\mathrm{d}\tilde{x} + \sqrt{2\pi}\frac{A}{K_{\mathrm{I}}} h(x). \tag{4}$$

For a homogeneous material, this equation admits a trivial solution, namely a straight crack path. To take into account spatial variations in the fracture properties of the material and describe the resulting perturbations of the crack trajectory, one introduces the stochastic term $\delta k_{\mathrm{II}}^{\mathrm{het}} = -K_{\mathrm{I}}\,\eta(x)/2$ that describes the local shearing resulting from the material microstructure. Note that perturbations $\delta k_{\mathrm{I}}(x)$ in the local tensile stress intensity factor do not affect the linear path equation (4) as they give rise to higher order terms proportional to $\delta k_{\mathrm{I}}(x)$ and the height perturbations $h(x)$. Finally, as the materials considered here have a random microstructure with a characteristic size ℓ, we assume an uncorrelated noise for length scales $\delta x \gg \ell$. Taking now into account $k_{\mathrm{II}} = k_{\mathrm{II}}^{\mathrm{hom}} + k_{\mathrm{II}}^{\mathrm{het}}$ to predict the kink angle from Eq. (2), one obtains

$$h'(x^+) = \frac{\mathrm{sign}\,(T)}{\sqrt{\mathcal{L}_1}} \int_{-\infty}^{x} \frac{h'(\tilde{x})}{\sqrt{x-\tilde{x}}}\mathrm{d}\tilde{x} + \mathrm{sign}\,(A)\frac{h(x)}{\mathcal{L}_2} + \eta(x), \tag{5}$$

where $\mathcal{L}_1 = \pi/8\,(K_{\mathrm{I}}/T)^2$ and $\mathcal{L}_2 = 1/\sqrt{2\pi}\,K_{\mathrm{I}}/|A|$ are structural length scales determined by the specimen geometry only. Their calculation for the experiments and the simulations performed in this study is detailed in Appendix B and their value is listed in Table I.

Contrary to the model proposed in Refs. [26, 27], we do not consider variations in elastic properties. This hypothesis significantly changes the nature of the crack path equation that is a first order differential equation for uniform elastic constant and of second order otherwise [26, 27]. In our model, the crack path perturbations result from the variations of fracture properties only. In the context of the consolidated granular solids considered in this study, these heterogeneities (embedded in the quenched noise $\delta k_{\mathrm{II}}^{\mathrm{het}}(x)$) result from the randomly oriented weak planes present in the granular microstructure. Note that a similar description was previously employed in the context of cracks propagating through brittle materials with random fracture properties [8, 12, 13].

To characterize the geometry of the predicted crack profiles, we calculate the correlations of the slopes that can be directly inferred from Eq. (5) as detailed in Appendix C. Since the first and the second term on the right hand side of Eq. (5) are inversely proportional to $\sqrt{\mathcal{L}_1} \gg \sqrt{\ell}$ and $\mathcal{L}_2 \gg \ell$, respectively, and therefore negligible, the correlation of the slopes is simply expressed as

$$\langle h'(x+\delta x)h'(x)\rangle_x \simeq \langle \eta(x+\delta x)\eta(x)\rangle_x. \tag{6}$$

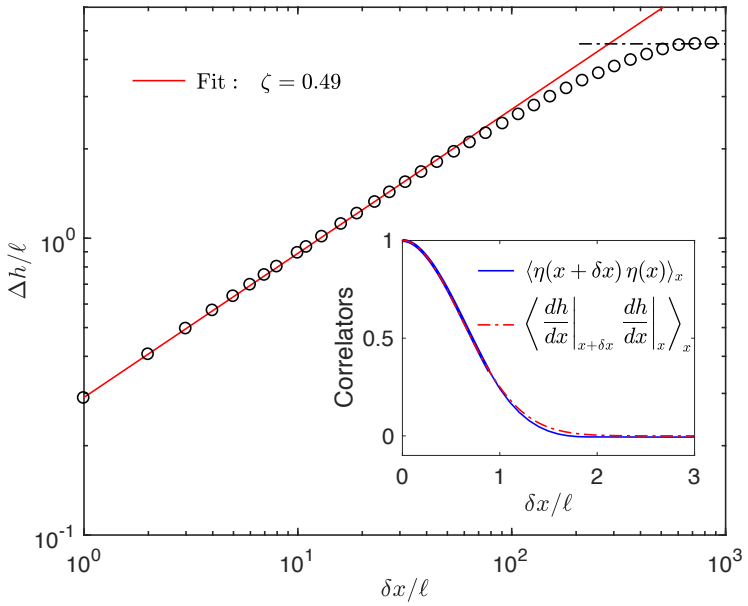

FIG. 10. Correlation function of the fracture profiles as predicted by the path equation (5) solved numerically. For $\delta x > \ell$, the cracks follow a random walk with exponent $\zeta = 0.49$ (red straight line). In the inset, the correlator of the slopes of the predicted fracture profiles is compared with the correlator of η describing the material microstructure.

Local slopes of the crack profile have therefore the same correlator as η and, as such, display no correlations for $\delta x \gg \ell$. This property defines a random walk: the predicted cracks are self-affine profiles with a roughness exponent close to the random walk prediction $\zeta_{\rm rw} = 1/2$, in excellent agreement with the experimental and numerical observations reported in Fig. 6. The Gaussian statistics of the experimental and computed crack profiles evidenced in Fig. 7 derive from the central limit theorem, as the height variation at a scale $\delta x \gg \ell$ decomposes as the sum of $\delta x/\ell$ uncorrelated height variations computed at a finer scale ℓ. To describe effects emerging from the finite specimen size, like the saturation of the roughness Δh observed in Fig. 6 for $\delta x \gtrsim 100\,\ell$, the path equation (5) is solved numerically using the parameter values listed in Table I. Using a short range disorder η of correlator $\langle \eta(x+\delta x)\eta(x)\rangle_x = \sigma^2\, e^{-(\delta x/\ell)^2}$ with amplitude $\sigma = \sqrt{\langle \eta^2(x)\rangle_x} = 1$, one predicts the correlation function of Fig. 10 which compares rather well with the simulation results in Fig. 6. The inset shows the correlator of the crack slopes predicted by our model which, as expected from Eq. (6), is close to the one of the disorder term η. This validates the assumption that the terms proportional to T and A in the path equation (5) do not significantly impact the scaling properties of the fracture profile as long as the sample dimensions (described through the length scales $\mathcal{L}_1$ and $\mathcal{L}_2$) are much larger than the characteric size ℓ of the microstructural heterogeneities.

V. DISCUSSION

Our experimental and numerical observations, supported by our LEFM-based theoretical model, indicate that brittle cracks follow a directed random walks in 2-D materials as long as the structural length scales $\mathcal{L}_1$ and $\mathcal{L}_2$ set by the fracture test geometry are much larger than the characteristic microstructural length ℓ. More specifically, crack trajectories are self-affine profiles with exponent $\zeta \simeq 0.5$ and a Gaussian statistics as long as the scale of observation is larger than ℓ. Then, how to explain the discrepancy with paper [28–30], wood [31] or nickel-based alloy samples [32] that display persistent fracture paths with $\zeta \simeq 0.6$–0.7?

A key assumption of our theoretical model is the scale separation $\ell \gg \ell_{\rm pz}$ between the characteristic size ℓ of the microstructural disorder and the extent $\ell_{\rm pz}$ of the fracture process zone along the propagation direction where non-linear damage processes take place. Indeed, LEFM assumes an elastic response everywhere in the material, and therefore $\ell_{\rm pz}$ is expected to be small with respect to any other length scale of the problem. This assumption is satisfied in the materials investigated here, as the cohesive zone lengths chosen in the simulations and estimated in the experiments are much smaller than the microstructural length ℓ. On the contrary, the extent of the fracture process zone does compare with the characteristic microstructural feature in paper ($\ell \simeq 100\ \mu$m $\lesssim \ell_{\rm pz} \simeq 1$ mm), wood ($\ell \simeq \ell_{\rm pz} \simeq 1$–$5$ mm) and nickel-based alloy ($\ell \simeq \ell_{\rm pz} \simeq 100\ \mu$m) for which a large exponent $\zeta \simeq 0.6$–0.7 was measured.

These observations lead us to conclude the following scenario:

- for $\ell_{\rm pz} \ll \ell$, crack paths can be accurately described by LEFM and follow a directed random walk with exponent $\zeta = 0.5$ in the limit of very large specimens, as shown in this study;
- for $\ell_{\rm pz} \gtrsim \ell$, the roughening process is dominated by the underlying damage mechanism that takes place within the process zone. As shown by Bouchbinder *et al.* [33], this crack growth mechanism leads to persistent crack paths with $\zeta \simeq 0.6$–0.7, in good agreement with the experimental observations in paper [28–30], wood [31] and alloy [32].

Interestingly, this scenario also accounts for the puzzling observation of random walk crack profiles with $\zeta \simeq 0.5$ in paper sheets perforated with holes [51], while fracture lines in virgin paper display $\zeta \simeq 0.65$ [28–30]. The upscaling of the characteristic size of the disorder, from the size of the fibers $\ell \simeq 100$ μm to the distance $\ell \simeq 1$ mm between holes, may have shifted the roughening mechanism from a damage coalescence driven process to the brittle mechanism described in this study. Note that this scenario applies to the roughness of cracks observed at scales larger than the grain size or the process zone size (whichever is larger). For example, at a very fine scale—$\delta x < \ell_{\rm pz}$ in the granular solids considered in this work—one may observe roughness features reminiscent of damage coalescence.

To conclude, we would like to highlight the remarkably simple features of brittle crack paths in large 2-D specimens that show a Gaussian statistics of height fluctuations and a roughness exponent close to the random walk prediction $\zeta_{\rm rw} = 1/2$. This behavior reminds the large scale roughness regime in 3-D solids that also display Gaussian statistics and mono-affine properties with $\zeta \simeq 0.4 - 0.5$ [9, 14, 16], and it can be easily distinguished from fractures dominated by damage coalescence that display complex multi-affine features with fat-tail statistics both in 2-D [46] and 3-D [16, 19, 52] materials. This simple scenario suggests that fracture roughness in both 2-D and 3-D may be broadly understood in terms of one or the other mechanism, with the major difference that the damage driven regime may extend to large scales in 2-D, but remains confined to small scales in 3-D. We hope that this work will help to develop new tools of quantitative fractography that translate statistical properties of fracture surfaces into meaningful quantities for engineering applications, in the spirit of recent works relating roughness and toughness [20, 21].

ACKNOWLEDGMENTS

It is a pleasure to thank Mokhtar Adda-Bedia, Elisabeth Bouchaud and Jean-Baptiste Leblond for fruitful discussions. Z.S. was financially supported by the Higher Education Commission, Pakistan. L.P. gratefully acknowledges the support of the city of Paris through the Emergence program.

Appendix A: Large scale simulations of intergranular failure through sequential polycrystalline analyses

In the sequential polycrystalline analysis approach, a simulation is split into a suitable number of sub-simulations. The approach is illustrated in Fig. 11 by means of a 90-grain topology embedded in the specimen in Fig. 4 that has been analyzed in three different ways. To build a reference set of results, the first simulation uses a discretization that resolves the cohesive zone along each grain boundary following the rules suggested by Shabir *et al.* [42]. The resulting crack path is depicted in Fig. 11(a), and Fig. 11(d) shows the corresponding load-displacement curve. With the results of the first analysis, all the grain boundaries that experienced a non-negligible opening have been used to define an active process zone.

In the second analysis, we allowed non-linearities from the cohesive law within the previously defined active process zone only. The grain boundaries outside this zone are given a high stiffness to simulate perfect bond. This analysis yielded the same crack path and load displacement curve as obtained in the first analysis. It can be therefore deduced that a mesh that resolves the cohesive zone is needed only in the active process zone to account for the non-linearities. The region outside the active process zone, exhibiting mostly a linear elastic behavior, can be discretized with a coarser mesh. Following this argument, in our third analysis we split the simulation into a sequence of sub-simulations. For the purpose of demonstrating the approach, we consider two sub-simulations as described in the following procedure.

1. A discretization that resolves the zohesive zone along each grain boundary as proposed in [42] is provided around the crack tip in the active process zone. Outside this region, at least two elements are provided along each grain boundary. Both regions can be seen in Figs. 11(b) and (c) for each sub-simulation.
2. When a crack tip reaches the end of an active process zone in the crack propagation direction, the simulation is stopped and the resulting crack profile is saved—the crack path obtained from simulation 1 is indicated by the red line in Fig. 11(b). The next sub-simulation is launched considering the saved crack profile from the previous

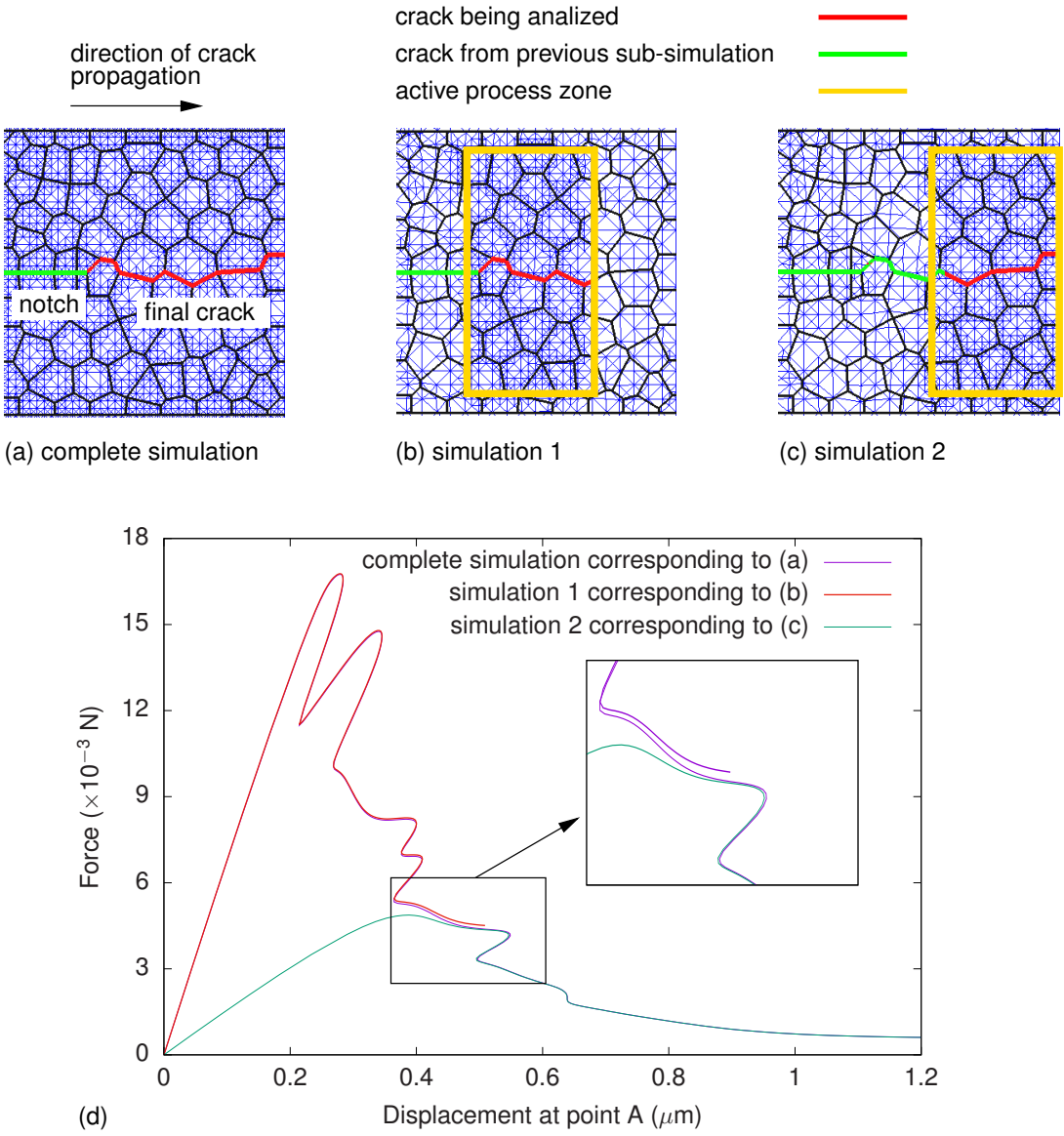

FIG. 11. Sequential polycrystalline analysis of a 90-grain topology: (a) discretized process zone with final crack path; (b and c) sub-simulation 1 and 2 with refined mesh in the active process zone—at least two elements along each grain boundary are provided outside the active process zone; (d) load-displacement curves corresponding to the simulations in (a), (b) and (c). Only the process zone, defined in Fig. 4, is shown in (a) to (c).

simulation—the green line in Fig. 11(c). A new crack tip is defined by reducing the length of the loaded crack profile such that the new tip is now at a position where the cohesive strength of the previous simulation would be negligible—the green line in Fig. 11(c) does not extend up to the upper end of the red line in Fig. 11(b). In other words, we make sure that nonlinear processes are accurately captured by enclosing nonlinear regions with an active process zone. We have found that an overlap of $\sim 2.5\,\ell$ between two consecutive active process zones satisfies this requirement with the current choice of cohesive law and parameters.

The sequential polycrystalline analysis yielded a crack path (Fig. 11(c)) identical to that obtained with the first monolithic analysis (Fig. 11(a)). The equivalence of the two approaches in delivering essentially the same results can also be appreciated from the load-displacement curves in Fig. 11(d). In this figure, the curves related to the two sub-simulations are basically indistinguishable from the curve from the first analysis in their respective domains. With regards to the stress field, we could hardly find any difference between the analyses.

With this approach, the large crack propagation simulations needed for the estimation of the roughness exponent can be carried out by considering a suitable number of computationally-doable sub-simulations. A typical example

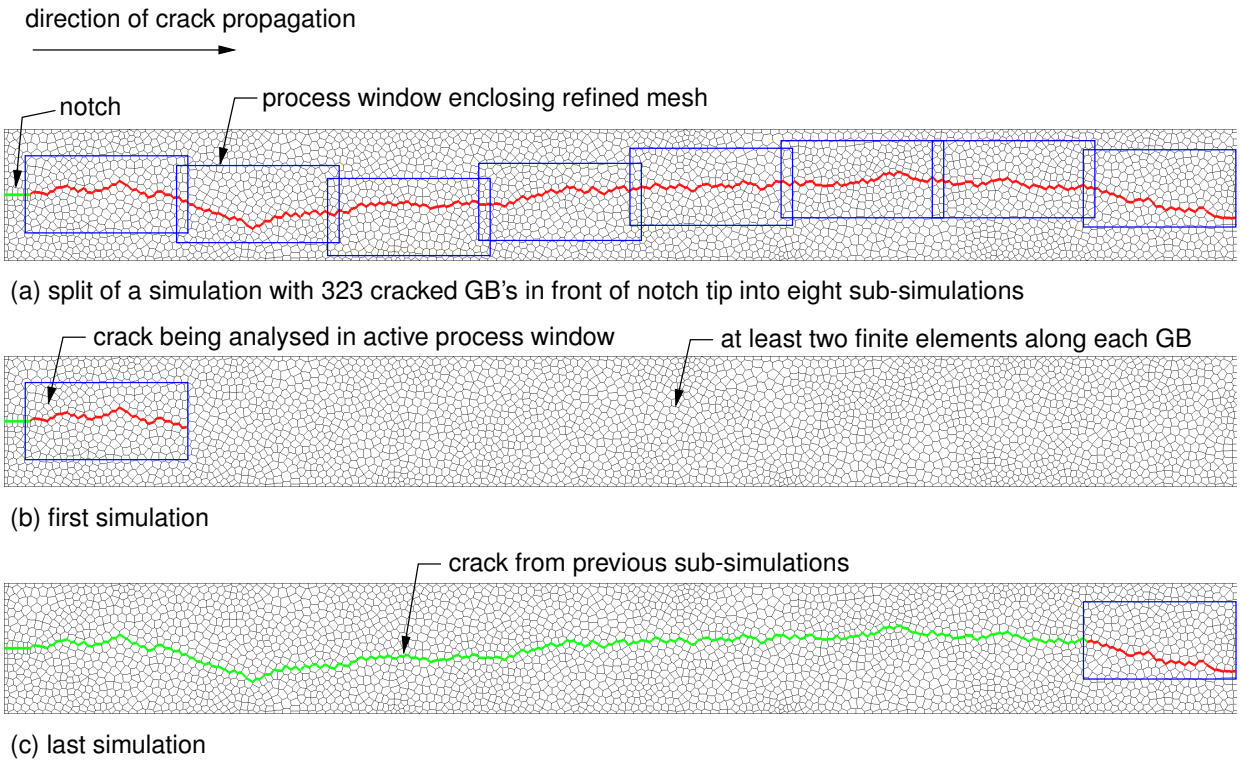

FIG. 12. Sequential polycrystalline analysis of a 3140-grain topology. Only the process zone is shown.

employing a 3140-grain topology and eight sub-simulations was shown in Fig. 5 and reproduced in Fig. 12(a) with the first and last sub-simulation reported in Figs. 12(b) and (c), respectively. The blue boxes in these figures are the active process zone which show the area where the crack is allowed to propagate within a sub-simulation. The corresponding load-displacement curves for the eight sub-simulations are reported in Fig. 13. From the inset in this figure, the complexity of the analysis, overwhelmed by many sharp snap-backs, can be easily recognized—it is worth noticing that each jump in the curve corresponds to the fracture of one grain boundary. Unlike adaptive refinement approaches, the only information that is transferred from simulation to simulation is the crack path.

Appendix B: Determination of the structural length scales $\mathcal{L}_1$ and $\mathcal{L}_2$

The structural length scales involved in the path equation (5) emerge from the specimen geometry and the boundary conditions. They are defined as

$$\begin{cases} \mathcal{L}_1 &= \dfrac{\pi}{8}\left(\dfrac{K_{\rm I}}{T}\right)^2, \\ \mathcal{L}_2 &= \dfrac{1}{\sqrt{2\pi}}\dfrac{K_{\rm I}}{|A|}. \end{cases} \tag{B1}$$

In these expressions, the stress intensity factor K_I, the T-stress and the parameter A correspond to the pre-factors in Williams' expansion

$$\sigma_{xx}(x) = \frac{K_{\rm I}}{\sqrt{2\pi x}} + T + A\sqrt{x} \tag{B2}$$

of the near tip stress parallel to the crack before considering geometrical perturbations of the crack profile [23, 49].

The value of $K_{\rm I}$, T and A, as well as the value of $\mathcal{L}_1^{\rm sim}$ and $\mathcal{L}_2^{\rm sim}$ for the specimen geometry and boundary conditions in Fig. 4 used in the simulations, are computed using the finite element method. Since both $\mathcal{L}_1$ and $\mathcal{L}_2$ are independent of the amplitude of the applied stress, we consider a unit applied stress normal to the crack propagation direction. The elements of the mesh are chosen so that their size decreases exponentially while approaching the crack tip,

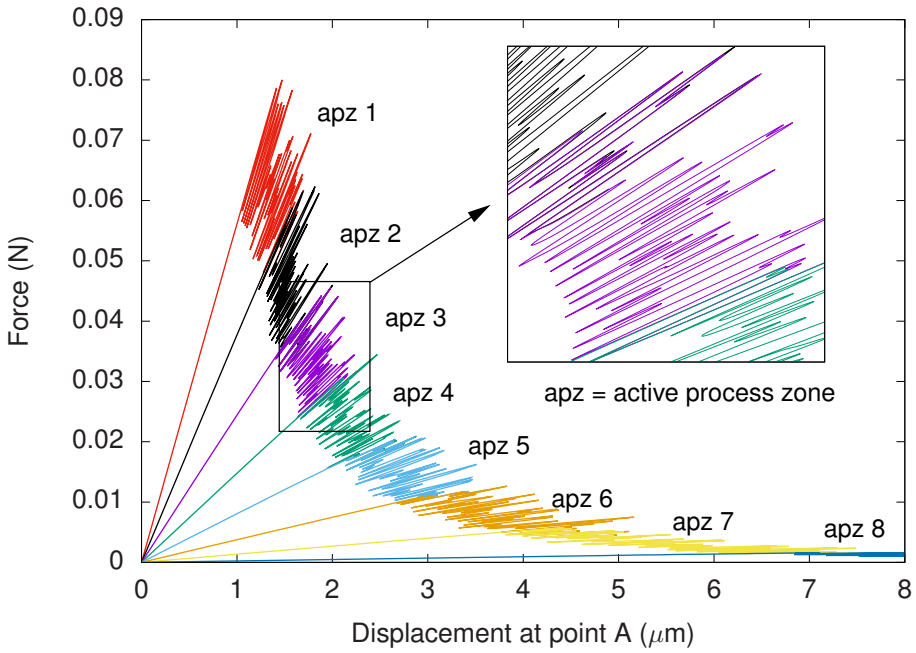

FIG. 13. Load-displacement curves obtained through sequential polycrystalline analysis for the 3140-grain topology depicted in Fig. 12.

down to a minimum element size of $10^{-9}\,W$ where W is the specimen width. This allows to capture the square root divergence of the stress field within reasonable computing times. The variations of $\sigma_{xx}(r)$ are then fitted using Williams' expansion (B2) following the procedure proposed in Ref. [53] and described next. First, $K_{\rm I}$ is obtained from the square root divergence of the stress in the near tip region. Then, the leading term $K_{\rm I}/\sqrt{2\pi x}$ of the stress field expansion is subtracted from the total stress so that the residual $\Delta\sigma_{xx}(x) = \sigma_{xx}(x) - K_{\rm I}/\sqrt{2\pi x}$ can be fitted by an affine function $\Delta\sigma_{xx} = T + A\sqrt{x}$ (see Fig. 14). This provides the value of T and A. Finally, Eqs. (B1) yield $\mathcal{L}_1^{\rm sim} = 85\,W$ and $\mathcal{L}_2^{\rm sim} \simeq W/3$ for the geometry considered in the simulations where the crack tip lies in the middle of the specimen. Using the actual size of the sample considered in the simulations, one gets $W \simeq 1000\,\ell$ where ℓ is the grain boundary length. This yields structural lengths $\mathcal{L}_1^{\rm sim} = 85\,000\,\ell$ and $\mathcal{L}_2^{\rm sim} \simeq 330\,\ell$ which, indeed, are much larger than the microstructural length. The same procedure is applied to determine $\mathcal{L}_1$ and $\mathcal{L}_2$ in the thin strip experiment.

To determine $\mathcal{L}_1^{\rm exp}$ and $\mathcal{L}_2^{\rm exp}$ in the case of the double torsion experiment shown in Fig. 2, we follow a different approach, as the bending conditions imposed to the specimen and the complex crack front geometry (see, e.g., [54]) would have required a full 3-D finite element analysis of the stress field in the crack tip region. Instead, we estimate these length scales from approximate formulas for $K_{\rm I}$, T and A. In the double torsion test used in our experiments, the stress intensity factor follows $K_{\rm I} \simeq \dfrac{(w_1 - w_2)P}{d^2\sqrt{W}}$ for a unperturbed straight crack [40]. An estimate of the T-stress can be obtained using the relation $T = \sigma_{xx}^{\rm (nc)} - \sigma_{yy}^{\rm (nc)}$ [49] where the superscript nc refers to the stress field calculated for the same geometry and boundary conditions, but without crack. As the boundary conditions are close to generate pure bending in the middle part of the specimen, the stress $\sigma_{xx}^{\rm (nc)}$ aligned with the crack propagation direction is close to zero while the stress $\sigma_{yy}^{\rm (nc)}$ can be estimated at the bottom surface of the specimen where the tensile state of stress drives the crack, leading to $T \simeq -\sigma_{yy}^{\rm (nc)} \simeq -\dfrac{(w_1 - w_2)P}{d^2 L}$, so that $\mathcal{L}_1^{\rm exp} \simeq L^2/W$ from Eq. (B1). To estimate $\mathcal{L}_2^{\rm exp}$, we take inspiration from other fracture tests. For example, in the thin strip geometry, one gets $\mathcal{L}_2 \simeq W/2$. Similarly, in the double cleavage drilled compression test analyzed in Ref. [53], the third order term, proportional to $A \sim 1/\mathcal{L}_2$ in Williams' expansion of the near tip field, is also set by the specimen width W. We assume a similar behavior for the bending test used in the experiments, yielding $\mathcal{L}_2^{\rm exp} \simeq W/2$. This relation is supported by the physical intuition that the term $h/\mathcal{L}_2$ in the path equation (5) should be relevant when the crack starts to feel the specimen boundary, i.e., for crack path excursions h of the same order as the specimen half-width. The values of the structural lengths expressed in terms of sample dimensions and microstructural length ℓ (i.e., the bead radius in the experiments and the grain boundary length in the simulations) as well as the signs of the T-stress and the parameter A are provided

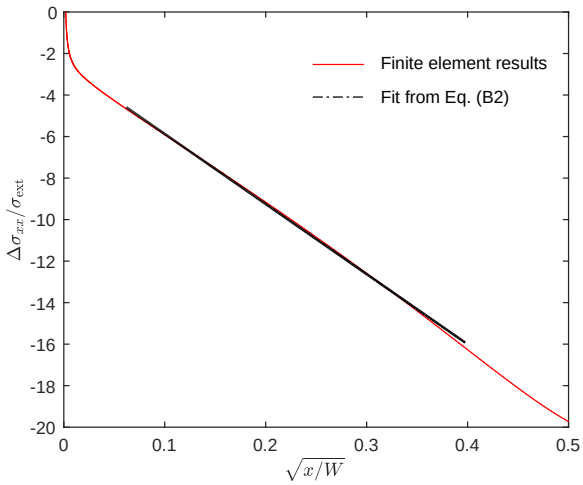

FIG. 14. Non-singular contribution $\Delta\sigma_{xx}(x) = \sigma_{xx}(x) - K_{\rm I}/\sqrt{2\pi x}$ of the stress that applies paralell to the crack in the thin strip geometry considered in the simulations (see Fig. 4). The fit by an affine function $\Delta\sigma_{xx} = T + A\sqrt{x}$ (see Eq. (B2)) provides the structural lengths $\mathcal{L}_1^{\rm sim}$ and $\mathcal{L}_2^{\rm sim}$ through Eq. (B1).

in Table I. It is worth noticing the opposite signs of the T-stress in the simulations and in the thin strip experiments that result from different boundary conditions: in the simulations the stress is imposed so that the boundary can move freely along the x direction, while in the experiments the vertical displacement is imposed by clamping the upper and lower part of the sample so that the strain $\varepsilon_{xx} = 0$ on the boundaries.

Appendix C: Perturbation analysis of the path equation

To gain insight into the path equation (5), we introduce the parameters

$$\epsilon_1 = \sqrt{\ell/\mathcal{L}_1} \quad \text{and} \quad \epsilon_2 = \ell/\mathcal{L}_2, \tag{C1}$$

equal to $\epsilon_1^{\rm sim} \simeq \epsilon_2^{\rm sim} \simeq 0.003$ in the simulations and $\epsilon_1^{\rm exp} \simeq 0.04$ and $\epsilon_2^{\rm exp} \simeq 0.01$ in the thin strip experiments. Employing the change of variables

$$\left\{ \begin{array}{lcl} w & = & x/\ell, \\ f(x) & = & h(x/\ell)/\ell, \\ \gamma(x) & = & \eta(x/\ell), \end{array} \right. \tag{C2}$$

the path equation (5) can be rewritten as

$$f'(w^+) = -\epsilon_1 \int_{-\infty}^{w} \frac{f'(\tilde{w})}{\sqrt{w-\tilde{w}}}\,\mathrm{d}\tilde{w} - \epsilon_2\, f(w) + \gamma(w) \tag{C3}$$

where f and w are dimensionless and provide the crack perturbation and the distance along the mean crack path in units of ℓ, respectively. The small values of ϵ_1 and ϵ_2 indicate that they can be used as small parameters to perturbatively solve the path equation in the context of the fracture tests performed in this work. Thus, we seek a solution in the form

$$f(w) = f^{(0)}(w) + \epsilon_1 f^{(1)}(w) + \epsilon_2 f^{(2)}(w). \tag{C4}$$

Inserting this expression into the path equation (C3) and separating zeroth order terms from those proportional to ϵ_1 or ϵ_2, we find

$$\begin{cases} f'^{(0)}(w^+) & = \gamma(w) \\ \epsilon_1 f'^{(1)}(w) + \epsilon_2 f'^{(2)}(w) & = -\epsilon_1 \mathcal{I}(w) - \epsilon_2 \dfrac{f^{(0)}(w)}{\ell} \end{cases} \tag{C5}$$

where $\mathcal{I}(w) = \displaystyle\int_{-\infty}^{w} \frac{f'^{(0)}(\tilde{w})}{\sqrt{w-\tilde{w}}}\,\mathrm{d}\tilde{w}$. In terms of the original variables, the zeroth order equation gives

$$h'^{(0)}(x^+) = \eta(x). \tag{C6}$$

We remind that the term η describes the local shear perturbations resulting from the material microstructure. We therefore expect that it behaves as a short range correlated quenched noise. As a result, the solution $h^{(0)}$ of the zeroth order equation predicts a directed random walk. This is consistent with the numerical and experimental observations reported in this study.

We now seek to determine the correlation function of the local slopes along the crack path which, using the decomposition (C4) expressed in terms of $h(x)$ as $h(x) = h^{(0)}(x) + \epsilon_1 h^{(1)}(x) + \epsilon_2 h^{(2)}(x)$, reads

$$\begin{aligned} C(\delta x) &= \langle h'(x)h'(x+\delta x)\rangle_x \\ &= \langle h'^{(0)}(x)h'^{(0)}(x+\delta x)\rangle_x \\ &+ \langle h'^{(0)}(x)\left[\epsilon_1 h'^{(1)}(x+\delta x) + \epsilon_2 h'^{(2)}(x+\delta x)\right]\rangle_x \\ &+ \langle h'^{(0)}(x+\delta x)\left[\epsilon_1 h'^{(1)}(x) + \epsilon_2 h'^{(2)}(x)\right]\rangle_x + ... \end{aligned} \tag{C7}$$

Since $\epsilon_1 \ll 1$ and $\epsilon_2 \ll 1$, the terms proportional to ϵ_1 and ϵ_2 can be neglected. With the aid of Eq. (C6), Eq. (C7) reduces to $C(\delta x) = C_\eta(\delta x) = \langle \eta(x)\eta(x+\delta x)\rangle_x$. The correlator of the local slopes therefore coincides with that of the quenched disorder which implies that it is close to zero for $\delta x > \ell$ as also observed in our experiments and simulations.

[1] D. Bonamy and E. Bouchaud, Phys. Rep. **498**, 1 (2011).
[2] M. J. Alava, P. K. Nukala, and S. Zapperi, Adv. Phys. **55**, 349 (2006).
[3] B. B. Mandelbrot, D. E. Passoja, and A. J. Paullay, Nature **308**, 721 (1984).
[4] E. Bouchaud, G. Lapasset, and J. Planès, Europhys. Lett. **13**, 73 (1990).
[5] L. Ponson, D. Bonamy, and E. Bouchaud, Phys. Rev. Lett. **96**, 035506 (2006).
[6] S. Zapperi, Eur. Phys. J. B **85**, 329 (2012).
[7] L. Ponson, Int. J. Frac. **201**, 11 (2016).
[8] S. Ramanathan, D. Ertas, and D. S. Fisher, Phys. Rev. Lett. **79**, 873 (1997).
[9] S. Morel, D. Bonamy, L. Ponson, and E. Bouchaud, Phys. Rev. E **78**, 016112 (2008).
[10] S. Morel, J. Schmittbuhl, J. M. Lopez, and G. Valentin, Phys. Rev. E **58**, 6999 (1998).
[11] S. Santucci, K. J. Måløy, A. Delaplace, J. Mathiesen, A. Hansen, J. Bakke, J. Schmittbuhl, L. Vanel, and P. Ray, Phys. Rev. E **75**, 016104 (2007).
[12] D. Bonamy, L. Ponson, S. Prades, E. Bouchaud, and C.Guillot, Phys. Rev. Lett. **97**, 135504 (2006).
[13] L. Ponson, Ann. Phys. **32**, 1 (2007).
[14] J. M. Boffa, C. Allain, and J. P. Hulin, Eur. Phys. J. Appl. Phys. **2**, 281 (1998).
[15] L. Ponson, H. Auradou, P. Vié, and J. P. Hulin, Phys. Rev. Lett. **97**, 125501 (2006).

[16] L. Ponson, H. Auradou, M. Pessel, V. Lazarus, and J.-P. Hulin, Phys. Rev. E **76**, 036108 (2007).
[17] T. Cambonie, J. Barés, M. L. Hattali, D. Bonamy, V. Lazarus, and H. Auradou, Phys. Rev. E **91**, 012406 (2015).
[18] D. Dalmas, A. Lelarge, and D. Vandembroucq, Phys. Rev. Lett. **101**, 255501 (2008).
[19] S. Vernède, L. Ponson, and J.-P. Bouchaud, Phys. Rev. Lett. **141**, 215501 (2015).
[20] A. Srivastava, L. Ponson, S. Osovski, E. Bouchaud, V. Tvergaard, and A. Needleman, J. Mech. Phys. Solids **63**, 62 (2014).
[21] S. Vernède and L. Ponson, International Patent PCT/15/514916 (2015).
[22] H. Larralde and R. C. Ball, Europhys. Lett. **30**, 87 (1995).
[23] B. Cotterell and J. R. Rice, Int. J. Frac. **16**, 155 (1980).
[24] M. Amestoy and J.-B. Leblond, Int. J. Solids Struc. **29**, 465 (1992).
[25] O. Obrezanova, A. B. Movchan, and J. R. Willis, J. Mech. Phys. Solids **50**, 57 (2002).
[26] E. Katzav, M. Adda-Bedia, and B. Derrida, Europhys. Lett. **78**, 46006 (2007).
[27] E. Katzav and M. Adda-Bedia, Phys. Rev. E **88**, 052402 (2013).
[28] L. I. Salminen, M. Alava, and K. J. Niskanen, Eur. Phys. J. B **2003**, 369 (2003).
[29] J. Kertesz, V. Horvath, and F. Weber, Fractals **1**, 67 (1993).
[30] M. Mallick, P. P. Cortet, S. Santucci, S. G. Roux, and L.Vanel, Phys. Rev. Lett. **98**, 255502 (2007).
[31] T. Engøy, K. J. Måløy, A. Hansen, and S. Roux, Phys. Rev. Lett. **73**, 834 (1994).
[32] S. Morel, T. Lubet, J. L. Pouchou, and J. M. Olive, Phys. Rev. Lett. **93**, 065504 (2004).
[33] E. Bouchbinder, J. Mathiesen, and I. Procaccia, Phys. Rev. Lett. **92**, 245505 (2004).
[34] I. Ben-Dayan, E. Bouchbinder, and I. Procaccia, Phys. Rev. E **74**, 146102 (2006).
[35] S. Zapperi, P. K. V. V. Nukala, and S. Šimunović, Phys. Rev. E **71**, 026106 (2005).
[36] P. K. V. V. Nukala, S. Zapperi, M. J. Alava, and S. Šimunović, Phys. Rev. E **78**, 046105 (2008).
[37] G. F. J., E. M., and P. J., Eng. Frac. Mech. **72**, 1268 (2005).
[38] G. I. Barenblatt, Adv. Appl. Mech. **7**, 55 (1962).
[39] B. K. Atkinson, J. Geophys. Res. **89**, 4077 (1984).
[40] A. G. Evans, J. Mater. Sci. **15**, 1137 (1972).
[41] A. Simone, C. A. Duarte, and E. Van der Giessen, Int. J. Numer. Meth. Engng **67**, 1122 (2006).
[42] Z. Shabir, E. Van der Giessen, C. A. Duarte, and A. Simone, Modelling Simul. Mater. Sci. Eng. **19**, 035006 (2011).
[43] X.-P. Xu and A. Needleman, J. Mech. Phys. Solids **42**, 1397 (1994).
[44] J. Schmittbuhl, J. P. Vilotte, and S. Roux, Phys. Rev. E **51**, 131 (1995).
[45] E. Bouchaud and L. Ponson, *Fracture mechanics of heterogeneous materials* (Wiley, Hoboken, in preparation).
[46] E. Bouchbinder, I. Procaccia, S. Santucci, and L. Vanel, Phys. Rev. Lett. **96**, 055509 (2006).
[47] L. Ponson, H. Auradou, M. Pessel, V. Lazarus, and J.-P. Hulin, Phys. Rev. E **76**, 036108 (2007).
[48] R. V. Gol'dstein and R. L. Salganik, Int. J. Frac. **10**, 507 (1974).
[49] A. B. Movchan, H. Gao, and J. R. Willis, Int. J. Solids Struct. **35**, 3419 (1998).
[50] M. L. Williams, J. Appl. Mech. **24**, 109 (1957).
[51] O. Ramos, P.-P. Cortet, S. Ciliberto, and L. Vanel, Phys. Rev. Lett. **110**, 165506 (2013).
[52] L. Ponson, Y. Cao, E. Bouchaud, V. Tvergaard, and A. Needleman, Int. J. Frac. **184**, 137 (2013).
[53] G. Pallares, L. Ponson, A. Grimaldi, M. Georges, G. Prevot, and M. Ciccotti, Int. J. Frac. **156**, 11 (2009).
[54] M. Ciccotti, J. Am. Ceram. Soc. **83**, 2737 (2000).